



Article

Terahertz Emission Spectroscopy of Ultrafast Coupled Spin and Charge Dynamics in Nanometer Ferromagnetic Heterostructures

Zhangshun Li ^{1,†}, Yexin Jiang ^{1,†} , Zuanming Jin ^{1,*}, Zhuoyi Li ², Xianyang Lu ^{2,*}, Zhijiang Ye ¹, Jin-Yi Pang ¹, Yongbing Xu ² and Yan Peng ^{1,*}

¹ Terahertz Technology Innovation Research Institute, Terahertz Spectrum and Imaging Technology Cooperative Innovation Center, Shanghai Key Lab of Modern Optical System, University of Shanghai for Science and Technology, Shanghai 200093, China

² Jiangsu Provincial Key Laboratory of Advanced Photonic and Electronic Materials, School of Electronic Science and Engineering, Nanjing University, Nanjing 210093, China

* Correspondence: physics_jzm@usst.edu.cn (Z.J.); xylyu@nju.edu.cn (X.L.); py@usst.edu.cn (Y.P.)

† These authors contributed equally to this work.

Abstract: Due to its high sensitivity and because it does not rely on the magneto-optical response, terahertz (THz) emission spectroscopy has been used as a powerful time-resolved tool for investigating ultrafast demagnetization and spin current dynamics in nanometer-thick ferromagnetic (FM)/heavy metal (HM) heterostructures. Here, by changing the order of the conductive HM coating on the FM nanometer film, the dominant electric dipole contribution to the laser-induced THz radiation can be unraveled from the ultrafast magnetic dipole. Furthermore, to take charge equilibration into account, we separate the femtosecond laser-induced spin-to-charge converted current and the instantaneous discharging current within the illuminated area. The THz emission spectroscopy gives us direct information into the coupled spin and charge dynamics during the first moments of the light–matter interaction. Our results also open up new perspectives to manipulate and optimize the ultrafast charge current for promising high-performance and broadband THz radiation.

Keywords: spintronic THz emitters; ultrafast demagnetization; spin-to-charge current conversion; THz emission spectroscopy



Citation: Li, Z.; Jiang, Y.; Jin, Z.; Li, Z.; Lu, X.; Ye, Z.; Pang, J.-Y.; Xu, Y.; Peng, Y. Terahertz Emission Spectroscopy of Ultrafast Coupled Spin and Charge Dynamics in Nanometer Ferromagnetic Heterostructures. *Nanomaterials* **2022**, *12*, 4267. <https://doi.org/10.3390/nano12234267>

Academic Editor: Rodolphe Antoine

Received: 3 November 2022

Accepted: 28 November 2022

Published: 30 November 2022

Publisher's Note: MDPI stays neutral with regard to jurisdictional claims in published maps and institutional affiliations.



Copyright: © 2022 by the authors. Licensee MDPI, Basel, Switzerland. This article is an open access article distributed under the terms and conditions of the Creative Commons Attribution (CC BY) license (<https://creativecommons.org/licenses/by/4.0/>).

1. Introduction

Laser-induced ultrafast magnetization phenomena in materials attracts strong interest from both basic knowledge and technology perspectives [1–5]. The ability to efficiently control the spin of ferromagnets on a femtosecond (fs) timescale paves the way to ultrafast optical writing of magnetic memory and data processing [6–10]. Although many experiments and theories have been presented lately, the clear physical mechanism of the processes occurring during the interaction of ultrashort laser pulses with the spin order remains largely unclear, even though understanding dynamics on this timescale is critical for both physical and practical insights into the spin diffusion, precession, relaxation, and spin–orbit interaction [11–15].

The key experimental techniques routinely employed so far are the time-resolved magneto-optical Kerr effect (TR-MOKE) [16,17] or soft X-ray pulses [18]. These techniques have provided invaluable information concerning the transient evolution of magnetization in magnetic materials on fs and longer timescales. However, both of these techniques, as based on the pump–probe cross-correlation, are inherently ambiguous towards the material response during the interaction of the laser pulse with the material. This is due to the zero-time ambiguity of the pump–probe measurement and the possible occurrence of coherent effects or artifacts between pump and probe pulses [5]. As the propagation

of terahertz (THz) waves in materials is mainly affected by the motion of the electrons, it provides the most direct way to probe the magneto-transport properties on an ultrafast time scale. Over the past years, THz time-domain spectroscopy (THz-TDS) has provided the opportunity for not only investigating biomedical systems [19,20], but also uncovering the spin dynamics in both antiferromagnetic [21–25] and ferromagnetic materials [26–30]. Furthermore, in contrast to the TR-MOKE method, THz emission spectroscopy does not rely on the magneto-optical response and has been used as a fingerprint identification of the ultrafast demagnetization [31,32], inverse spin Hall effect (ISHE) [33–35], inverse spin-orbit torque [36], inverse Rashba–Edelstein effect (IREE) [37–39], and anomalous Hall effect (AHE) [40]. In addition, THz emission spectroscopy has the capability of small magnetic field change detection in the μT range [41] and near-field imaging with subwavelength resolution [42].

It is widely understood that the ultrafast response of a laser-excited pure ferromagnetic system is dominated by the ultrafast demagnetization (UDM) [1,43]. In a ferromagnetic (FM) thin film, the excess energy of laser-excited hot electrons is transferred to spin and lattice subsystems, leading to the local magnetic dipole THz radiation, $E(t) \propto \frac{\partial^2 M}{\partial t^2}$ [31,32,44], where M is the magnetization of the FM layer. On the other hand, the spin-to-charge current conversion (SCC) via ISHE, IREE, or AHE converts the spin current (j_s) into a charge current (j_c) via spin-orbit coupling, $j_c \propto j_s \times \frac{M}{|M|}$. Such a response acts as an electronic dipole THz radiation, $E(t) \propto \frac{\partial j_c}{\partial t}$ [45–47]. Remarkably, the working principle of the THz radiation remains entangled with the microscopic origin on how an ultrafast laser pulse modifies the magnetic system after fs laser excitation. In addition, the far field detection of THz emission does not give access to the exact current distribution in the emitter. To disentangle the physical origins is also crucial to maximize the generation efficiency of THz pulses.

In this work, we use time-resolved THz emission spectroscopy to study the spin and charge dynamics in laser-excited MgO (substrate)/Pt/CoFeB/Ta and MgO/Ta/CoFeB/Pt heterostructures. Such a choice of samples allowed us to accurately trace the measured THz emission back to the transients of UDM and SCC contributions at any moment during and after the interaction of the fs laser pulse with the sample. As a result, we gain direct access to the zero-time response of the laser-excited transient spin voltage dynamics in ferromagnetic/heavy metal (FM/HM) heterostructures, which is knowledge difficult to obtain by any other methods. Our work demonstrates potential for an ultrafast THz magnetometer and spintronic THz emitter.

2. Materials and Methods

2.1. Thin Films Preparation

Two types of samples were prepared. Here, 6 nm-thick Pt(2)/CoFeB(2)/Ta(2) and Ta(2)/CoFeB(2)/Pt(2) heterostructure films were grown on single-crystalline MgO (100) substrates. For the Pt/CoFeB/Ta sample, the 2 nm-thick Pt layer was firstly deposited by magnetron sputtering on a MgO substrate. Then, a 2 nm-thick CoFeB layer was deposited on the Pt layer, and a 2 nm-thick Ta layer was deposited on the CoFeB. The deposition rate of the Pt (the DC power was 10 W) layer, the CoFeB (the DC power was 10 W) layer, and the Ta (the DC power was 10 W) layer were 0.3, 0.15, and 0.3 Å/s at 7×10^{-3} Torr, respectively. The samples were annealed in situ after deposition at 250 °C for 60 min. For the Ta/CoFeB/Pt sample, the deposition process is similar under identical preparation conditions.

2.2. Terahertz Emission Spectroscopy

In Figure 1a,b, the conceptual schematic of our THz emission spectroscopy is shown. The sample is nearly homogeneously pumped by a normal incident of 800 nm (photon energy of 1.55 eV), pulse duration of 55 fs, and a repetition rate of a 1 kHz optical pulse. The beam is split into a pump beam and a probe beam for THz detection. The pump beam is angled at a normal incident onto the samples. The magnetization of the sample was set by an applied external magnetic field parallel to the y -axis (in-plane). The amount

of externally applied magnetic field was kept ~ 200 mT (sufficient to saturate the CoFeB layer). As the heterostructure is thinner than the laser penetration depth (~ 20 nm) [48], the excitation of hot electrons can be assumed to be homogeneous across the thickness of the film. We analyze the THz emissions from both SCC and UDM contributions by measuring the far-field free-space electro-optic sampling (EOS). The linearly-polarized THz emission was collected by a parabolic mirror and detected by a 1 mm-thick $\langle 110 \rangle$ ZnTe crystal gated by 55 fs, 800 nm laser pulses, using two parabolic mirrors. A chopper modulates the pump laser beam with a frequency of 0.5 kHz. The emitted THz pulses are sampled by delaying the probe laser beam time, and the amplified signal is recorded by a lock-in amplifier. All the measurements were performed at room temperature, and the spectrometer was purged with dry air to avoid the THz absorption by atmospheric water.

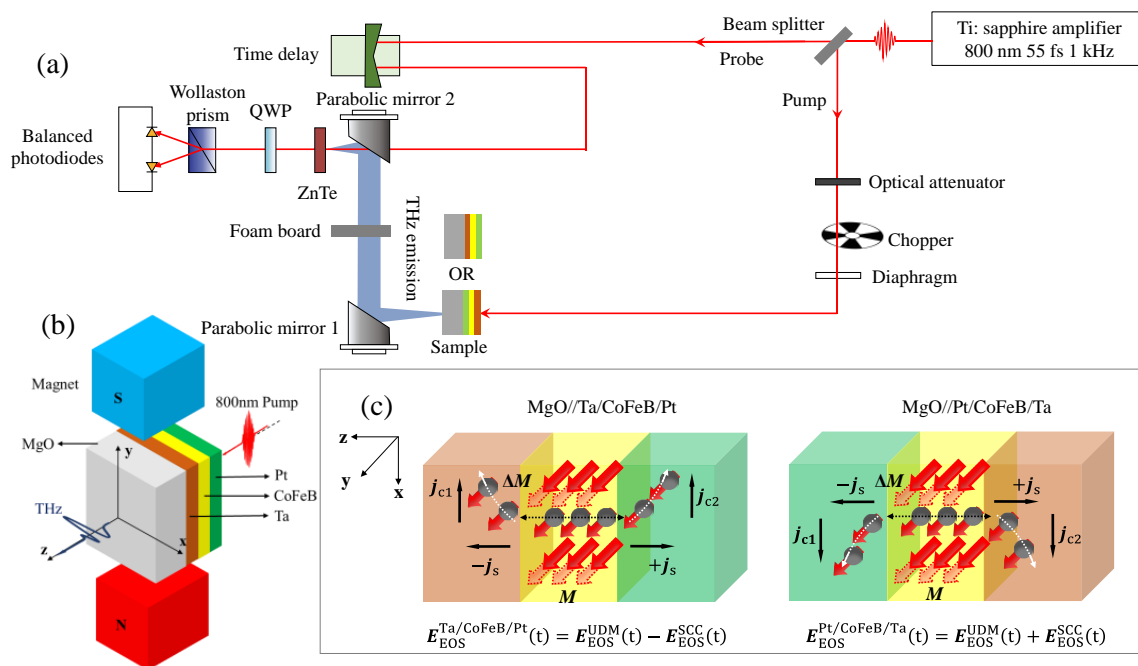


Figure 1. Generation of THz radiation from trilayer MgO//Pt/CoFeB/Ta and MgO//Ta/CoFeB/Pt stacks. (a) Schematic geometry for the THz emission spectroscopy in the transmission configuration. (b) The trilayer structure is excited by an 800 nm fs pump pulse and applied in-plane magnetic field of ± 200 mT. (c) Physical origins of SCC- and UDM-based THz generations. The black circles with arrows show the electrons with spins. The light red arrow and solid red arrow represent the magnetization M of the CoFeB layer, before and after ultrafast demagnetization, respectively. The black dotted arrows represent the diffusion of spin currents toward the Ta or Pt layer. The white dotted arrows represent the deflection and conversion of spin currents $\pm j_s$ into charge currents j_c in both the Pt and Ta layers.

Figure 1c shows that the excitation induces a transient spin voltage that launches spin currents flowing from CoFeB to Ta and from CoFeB to Pt. The trilayer emitter converts the bidirectional spin currents ($-j_s$ and $+j_s$) flowing into the lateral charge currents j_c within Ta and Pt, due to the ISHE. The time-varying j_c perpendicular to the j_s (scales with the M of CoFeB) and the direction of M gives rise to the emission of THz transients. We chose Ta and Pt because their signs of the spin Hall angle are opposite and, thus, their THz emissions add up [49]. Since the thickness of the used materials is small (nanometers), the THz radiations originating from the two HM layers have a negligible phase difference. In addition, a sizable contribution coming from the time-dependent UDM is also expected [31,32,50].

3. Results and Discussion

According to the experimental scheme shown in Figure 1, Figure 2a shows the typical time-domain THz EOS signals, $E_{\text{EOS}}(t)$, generated from both Pt/CoFeB/Ta and Ta/CoFeB/Pt stacks at a pump fluence of 1.0 mJ/cm^2 . Both THz transients are inverted symmetrically, as the direction of M is reversed with an external magnetic field of $\pm 200 \text{ mT}$. The polarization of the emitted THz pulses for both samples follows the direction perpendicular to M (along the y -axis), which indicates a strong connection between the THz emission and the magnetic order. We have also measured the THz emission of a 0.5 mm -thick ZnTe reference emitter under the same excitation condition. As shown in Figure 2b, the normalized Fourier spectra $|E_{\text{EOS}}(\omega)|$ versus frequency $\omega/2\pi$ of ZnTe covers a slightly higher range of frequencies, as compared with the trilayer stacks.

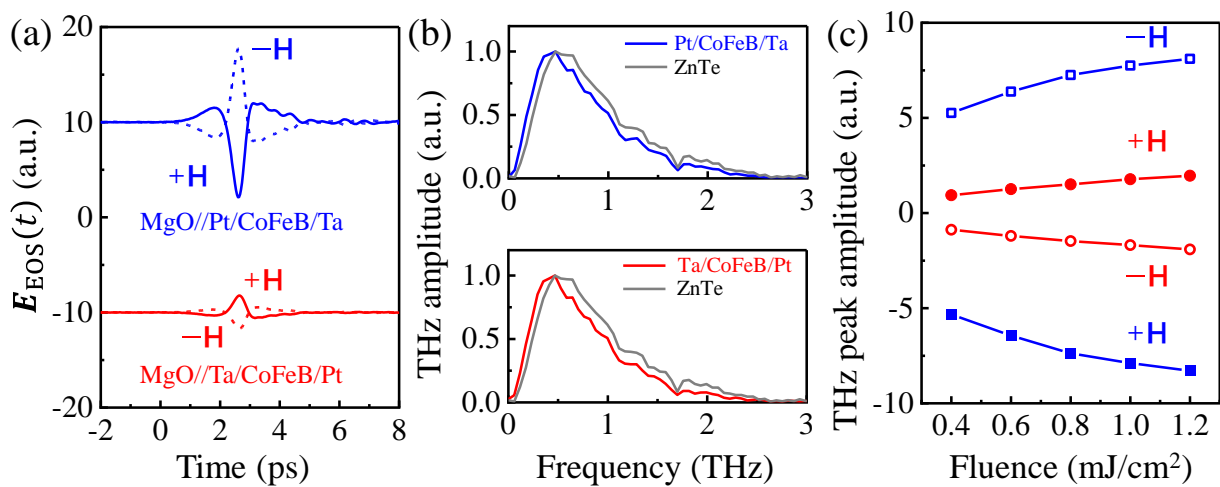


Figure 2. Terahertz waveforms at the different excitation geometries. (a) THz EOS waveforms $E_{\text{EOS}}(t)$ of the photoexcited MgO//Pt/CoFeB/Ta and MgO//Ta/CoFeB/Pt stacks. The zero-time delay corresponds to the arbitrary starting point. (b) The corresponding normalized Fourier transform of (a). The light-gray curve is the THz emission from a ZnTe crystal. (c) The pump fluence-dependence of THz peak amplitude from two samples at $\pm H$. Damage is not observed in the samples at the maximum pump fluence used here.

Figure 2a shows that the polarity of THz emissions in the Pt/CoFeB/Ta is found to reverse its sign, compared with the Ta/CoFeB/Pt, under the same experimental conditions. Given that the optical absorbance does not depend on the order of the sample, thus, a direction-dependent mechanism explains such polarity reversal of the THz emitted field. As shown in Figure 1c, by reversing the order of the Ta and Pt layer, the SCC model predicts a polarity reversal of the THz radiation owing to a reversion of charge currents within bilateral HM layers. Figure 2c shows that the THz peak amplitude increases with increased pump fluence and then reaches saturation. More THz waveforms at different pump fluences can be found in the Supplementary Materials.

It is also noted that the absolute value of THz signal from Pt/CoFeB/Ta is larger than that from Ta/CoFeB/Pt. That means the far-field $E_{\text{EOS}}(t)$ signals for two samples include both SCC and UDM contributions. Under the simplified assumption that the polarity of the THz emission by SCC is opposite for two samples, the UDM contribution does not change under the fixed magnetic field. Thus, $E_{\text{EOS}}^{\text{Pt/CoFeB/Ta}}(t) = E_{\text{EOS}}^{\text{UDM}}(t) + E_{\text{EOS}}^{\text{SCC}}(t)$ and $E_{\text{EOS}}^{\text{Ta/CoFeB/Pt}}(t) = E_{\text{EOS}}^{\text{UDM}}(t) - E_{\text{EOS}}^{\text{SCC}}(t)$. Therefore, the distinct contributions of UDM- and SCC-based THz emission can be expressed as follows:

$$E_{\text{EOS}}^{\text{UDM}}(t) = \left(E_{\text{EOS}}^{\text{Pt/CoFeB/Ta}}(t) + E_{\text{EOS}}^{\text{Ta/CoFeB/Pt}}(t) \right) / 2 \quad (1)$$

$$E_{\text{EOS}}^{\text{SCC}}(t) = \left(E_{\text{EOS}}^{\text{Pt/CoFeB/Ta}}(t) - E_{\text{EOS}}^{\text{Ta/CoFeB/Pt}}(t) \right) / 2 \quad (2)$$

Figure 3a,b plots the $E_{\text{EOS}}^{\text{UDM}}(t)$ (red) and $E_{\text{EOS}}^{\text{SCC}}(t)$ (blue) in the Pt/CoFeB/Ta and Ta/CoFeB/Pt samples. The THz peak amplitude by $E_{\text{EOS}}^{\text{UDM}}(t)$ reaches around 37% in magnitude compared with $E_{\text{EOS}}^{\text{SCC}}(t)$, which is consistent with the result reported by Liu et al. [51]. The most remarkable finding is that THz emission efficiency of a trilayer stack can be improved by optimizing the order of the Pt and Ta layers. Note also that the normalized UDM- and SCC-based THz emissions exhibit similar temporal waveforms on the picosecond time scales (inset of Figure 3a) and spectrum on the frequency domain (Figure 3c). In Figure 3d, both UDM and SCC contributions are shown as functions of pump fluences from 0.4 to 1.2 mJ/cm². Both SCC and UDM increase with the pump fluence, indicating that (1) hot electron transport is not hindered by the interface between CoFeB and HM layers, and (2) UDM-based THz emission is proportional to the magnitude of ultrafast demagnetization, before optical damage. All the experimental observations are consistent with the result reported by Rouzgar et al., and strongly demonstrate that SCC and UDM are driven by the same force, the transient spin voltage [52–54], $\dot{M} \propto j_s \propto \mu^\uparrow - \mu^\downarrow$, where μ^\uparrow and μ^\downarrow are the chemical potentials of majority- and minority-spin electrons in the FM layer, respectively.

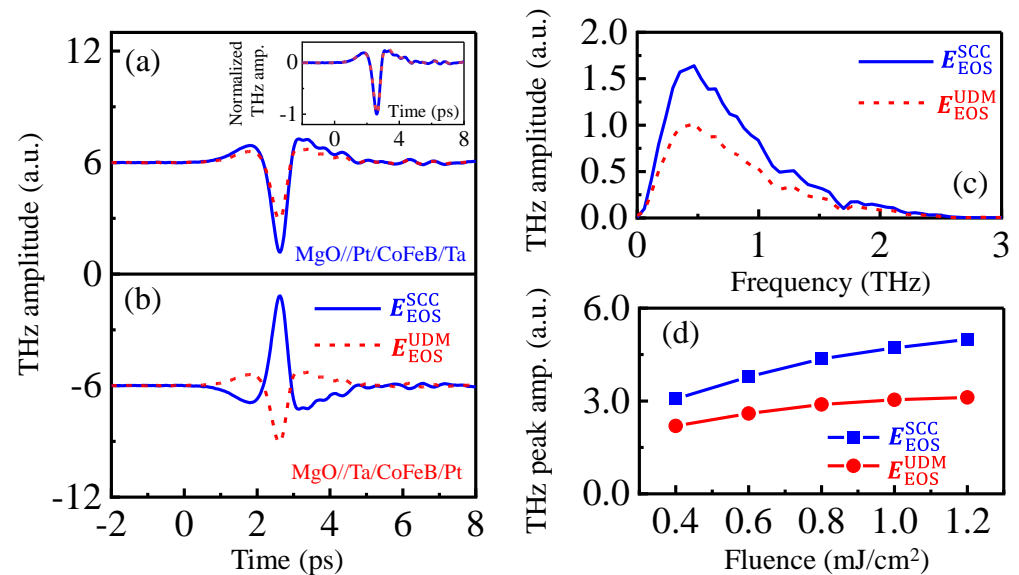


Figure 3. The $E_{\text{EOS}}(t)$ is decomposed into SCC and UDM contributions. The temporal $E_{\text{EOS}}^{\text{SCC}}(t)$ and $E_{\text{EOS}}^{\text{UDM}}(t)$ obtained in (a) Pt/CoFeB/Ta and (b) Ta/CoFeB/Pt, with a fluence of 1.0 mJ/cm². Inset shows the normalized $E_{\text{EOS}}^{\text{SCC}}(t)$ and $E_{\text{EOS}}^{\text{UDM}}(t)$. (c) The corresponding Fourier transforms of $E_{\text{EOS}}^{\text{SCC}}(t)$ and $E_{\text{EOS}}^{\text{UDM}}(t)$ of (a). (d) The THz peak amplitudes of SCC and UDM contributions versus pump fluence.

Note that the measured $E_{\text{EOS}}(\omega)$ are the convolution of the transient THz field at the emitter $E_{\text{emit}}(\omega)$ with the response function of our measurement setup $H_{\text{spectr}}(\omega)$ [55,56], $E_{\text{EOS}}(\omega) = E_{\text{emit}}(\omega) \times H_{\text{spectr}}(\omega)$, where $H_{\text{spectr}}(\omega)$ accounts for the propagation function of the THz pulse from the emitter to the EOS detector (see Supplementary Materials for details). Thus, we further calculate the near-fields of the emitted THz radiation $E_{\text{emit}}(t, \pm M)$ from the measured $E_{\text{EOS}}(t, \pm M)$, as shown in Figure 4a. As we are only interested in odd effects in the sample magnetization, we, thus, focus on the signal $E_{\text{emit}}^{\text{SCC}}(t) = \frac{E_{\text{EOS}}^{\text{SCC}}(t, +M) - E_{\text{EOS}}^{\text{SCC}}(t, -M)}{2}$, as shown in Figure 4b, which minimizes the artifacts of non-magnetic origin.

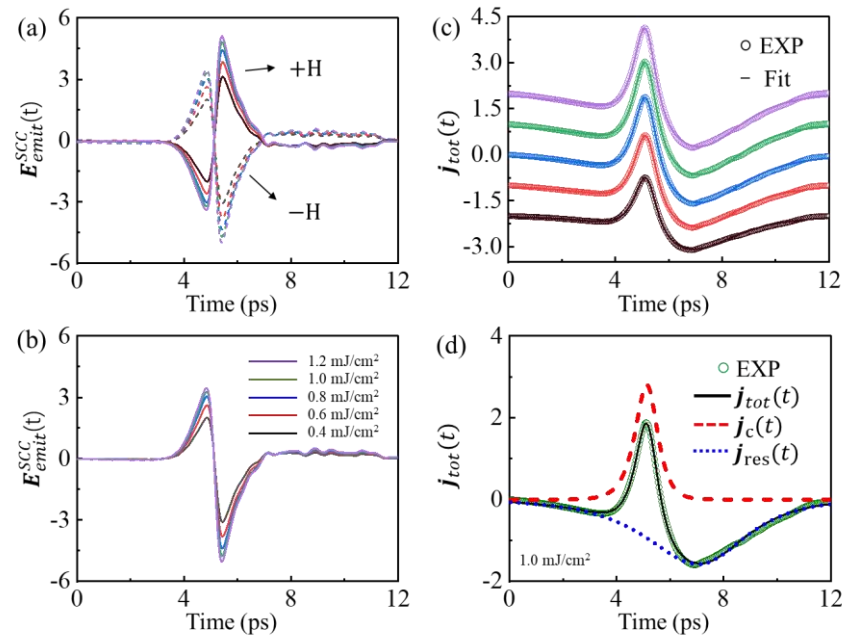


Figure 4. (a) The near-fields of the emitted THz radiation $E_{EOS}^{SCC}(t)$ for opposite applied magnetic fields with different pump fluences. (b) The difference $E_{emit}^{SCC}(t) = \frac{E_{EOS}^{SCC}(t, +M) - E_{EOS}^{SCC}(t, -M)}{2}$ odd in M . (c) The temporal profiles for charge current $j_{tot}(t)$ (vertical offset for clarity). The solid lines are the fits of Equation (4). (d) The complete charge current dynamics $j_{tot}(t)$ comprise both photoinduced SCC current $j_c(t)$ and restoration current $j_{res}(t)$, as shown by the red dashed and blue dotted line, respectively.

According to the charge conservation, the photoinduced SCC current j_c works as a current source, which charges a capacity within the illuminated area. The system is transiently charged locally. Then, the capacity will be discharged, which leads to a restoration of charge neutrality current j_{res} , which is dependent on the resistance of the surrounding material [57]. Therefore, the dynamics of total charge current is as follows:

$$j_{tot}(t) = j_c(t) + j_{res}(t) \tag{3}$$

The preceding equation describes a restoration of a charged state to a charge neutrality state. Figure 4c shows the measured total charge current transients $j_{tot}(t)$, which is proportional to the time integration of the THz near-fields in Figure 4b. The $j_{tot}(t)$ pulse consists of a positive peak followed by a negative one, which changes sign around 1.4 ps after onset. To gain more insight into our data, $j_{tot}(t)$ is fitted by a current profile [58,59], as follows:

$$j_{tot}(t) = \sum_{i=c, res} A_i \frac{e^{\alpha_i}}{e^{\alpha_i} + 1} \times e^{\beta_i} \tag{4}$$

where $\alpha_i = \frac{(t - t_{0,i}) - \tau_{rise, i}/2}{\tau_{rise, i}/4}$, $\beta_i = -\frac{t - t_{0,i}}{\tau_{decay, i}}$. Here, $\tau_{rise, i}$ and $\tau_{decay, i}$ are the rise and decay time constants of $j_{i=c, res}$, respectively. Furthermore, A_i and $t_{0, i}$ are the amplitude and time at peak of the current profile, respectively. The solid curves show the fitting results for different pump fluences. To aid comparison, the individual $j_c(t)$ (red dashed curve) and $j_{res}(t)$ (blue dotted curve) are separated, as shown in Figure 4d. In the beginning, the system response $j_{tot}(t)$ rises rapidly with the slope of $j_c(t)$. After a very short time, the $j_{tot}(t)$ decreases and change the sign, due to a negative contribution of $j_{res}(t)$. This restoration current is asymmetric around its peak, and the peak of $j_{res}(t)$ is slightly delayed with respect to the peak of $j_c(t)$. More figures of individual current dynamics at different pump fluences can be seen in the Supplementary Materials.

Figure 5 summarizes the extracted A_i , $t_{0,i}$, $\tau_{rise,i}$, and $\tau_{decay,i}$ of two current pulses versus the pump fluence. Figure 5a shows that the larger the pump fluence, the higher the amplitude of the currents of $j_c(t)$ and $j_{res}(t)$. This is a trivial consequence of the fact that due to the linear relationship between j_c and j_s , the increase in amplitude results from an increased excited spin current density upon deposition of the pump-pulse energy. Importantly, we observe the different time positions of $j_c(t)$ and $j_{res}(t)$ with different pump fluences. The $t_{0,c}$ for $j_c(t)$ is observed as being pump fluence-independent. On the other hand, the $t_{0,res}$ of $j_{res}(t)$ is slightly increased with the increase in pump fluence (Figure 5b). Figure 5 c,d shows that the rise and decay time constants of the charge currents are nearly pump fluence-independent. Here, $\tau_{rise} = 0.74 \pm 0.002$ ps and $\tau_{decay} = 0.33 \pm 0.005$ ps of $j_c(t)$ correspond to the timescale of transient spin currents, which are much faster than the 3.10 ± 0.005 ps and 1.33 ± 0.090 ps of $j_{res}(t)$. The rise and decay of the $j_{res}(t)$ mainly depends on the conductivity of the heterostructure. Therefore, a more proper consideration of the complex interplay between spin voltage profile, spin-to-charge conversion, and material properties is required to maximize and shape the THz emissions [60], which will be our future research focus.

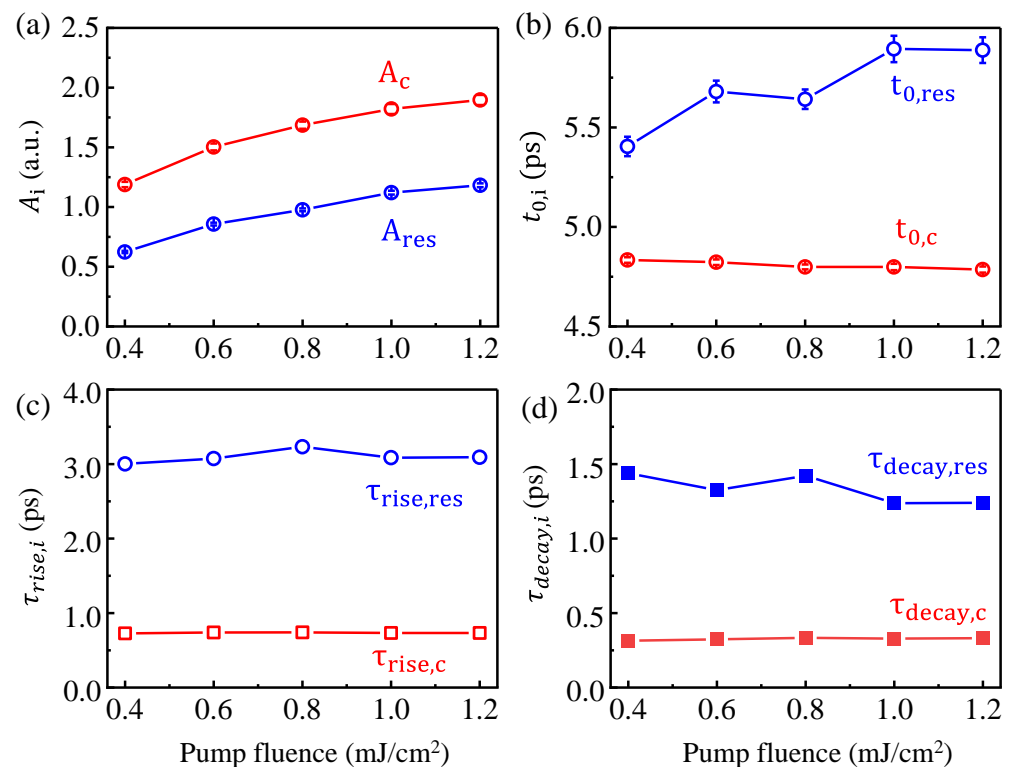


Figure 5. Pump fluence evolutions of (a) the amplitude and (b) time at peak of the $j_c(t)$ and $j_{res}(t)$ current profiles. Pump fluence-dependent (c) rise and (d) decay time constants of $j_c(t)$ and $j_{res}(t)$, respectively.

4. Conclusions

In summary, we have shown that high-performance broadband THz emission arises from both the magnetic dipolar radiation due to the ultrafast demagnetization and transient current radiation due to the spin–charge conversion. We find that the UDM contribution has the same time evolution as the SCC one, suggesting that they are driven by the same force, namely a generalized spin voltage. Finally, by taking the charge equilibration into account, we found that the THz generation depends on the overall superimposed fs laser-induced spin-to-charge converted current and an instantaneous backflow current. Our analysis distinguishes the contributions from the SCC and backflow charge current, which is essential to the underlying spin dynamics and optimization of spintronic THz emitters.

Supplementary Materials: The following supporting information can be downloaded at: <https://www.mdpi.com/xxx/s1>, Figure S1: (a) THz EOS waveforms $E_{\text{EOS}}(t)$ at different pump fluences for two samples. (b) and (c) are the Fourier transform of Pt/CoFeB/Ta and Ta/CoFeB/Pt in (a), respectively. Solid lines and dotted lines are the data measured with +H and −H, respectively; Figure S2: The fittings of charge currents with $j_c(t)$ and $j_{\text{res}}(t)$ contributions at difference pump fluence range from 0.4 mJ/cm² to 1.2 mJ/cm².

Author Contributions: Conceptualization, Z.J. and X.L.; data curation, Z.L. (Zhangshun Li), Y.J., Z.L. (Zhuoyi Li) and Z.Y.; formal analysis, Z.L. (Zhangshun Li), Y.J. and X.L.; funding acquisition, Y.X. and Y.P.; investigation, J.-Y.P.; methodology, Z.L. (Zhangshun Li), Z.J. and Y.P.; project administration, Y.P.; resources, Z.J., X.L. and Y.P.; software, Z.Y. and J.-Y.P.; supervision, Z.J. and Y.X.; visualization, Z.L. (Zhangshun Li) and Z.J.; writing—original draft, Z.L. (Zhangshun Li) and Z.J.; Writing—review and editing, Z.J., X.L. and Y.P. All authors have read and agreed to the published version of the manuscript.

Funding: This work is supported by the National Natural Science Foundation of China (NSFC, Grants No. 61988102, No. 61975110, No. 61735010, and No. 12104216); the 111 Project (Grant No. D18014); the Key project supported by Science and Technology Commission Shanghai Municipality (Grant No. YDZX20193100004960). The Science and Technology Commission of Shanghai Municipality (No.22JC1400200). General Administration of Customs People’s Republic of China (Grant No. 2019HK006). The Natural Science Foundation of Jiangsu Province of China (No. BK20200307). The National Key Research and Development Program of China (Grant No. 2021YFB3601600). Finally, JYP is also supported by the National Natural Science Foundation of China NSFC Grant No.12135011.

Institutional Review Board Statement: Not applicable.

Informed Consent Statement: Not applicable.

Data Availability Statement: The data of this study are available in the article, Supplementary Materials and upon request to the authors.

Conflicts of Interest: The authors declare no conflict of interest.

References

1. Beaulieu, E.; Merle, J.C.; Daunois, A.; Bigot, J.Y. Ultrafast spin dynamics in ferromagnetic nickel. *Phys. Rev. Lett.* **1996**, *76*, 4250–4253. [[CrossRef](#)]
2. Kirilyuk, A.; Kimel, A.V.; Rasing, T. Ultrafast optical manipulation of magnetic order. *Rev. Mod. Phys.* **2010**, *82*, 2731–2784. [[CrossRef](#)]
3. Kimel, A.V.; Kirilyuk, A.; Usachev, P.A.; Pisarev, R.V.; Balbashov, A.M.; Rasing, T. Ultrafast non-thermal control of magnetization by instantaneous photomagnetic pulses. *Nature* **2005**, *435*, 655–657. [[CrossRef](#)] [[PubMed](#)]
4. Zhang, G.P.; Hübner, W.; Lefkidis, G.; Bai, Y.H.; George, T.F. Paradigm of the time-resolved magneto-optical Kerr effect for femtosecond magnetism. *Nat. Phys.* **2009**, *5*, 499–502. [[CrossRef](#)]
5. Bigot, J.Y.; Vomir, M.; Beaulieu, E. Coherent ultrafast magnetism induced by femtosecond laser pulses. *Nat. Phys.* **2009**, *5*, 515–520. [[CrossRef](#)]
6. Vahaplar, K.; Kalashnikova, A.M.; Kimel, A.V.; Hinzke, D.; Nowak, U.; Chantrell, R.; Tsukamoto, A.; Itoh, A.; Kirilyuk, A.; Rasing, T. Ultrafast path for optical magnetization reversal via a strongly nonequilibrium state. *Phys. Rev. Lett.* **2009**, *103*, 117201. [[CrossRef](#)]
7. Lambert, C.H.; Mangin, S.; Varaprasad, B.S.D.C.S.; Takahashi, Y.K.; Hehn, M.; Cinchetti, M.; Malinowski, G.; Hono, K.; Fainman, Y.; Aeschlimann, M.; et al. All-optical control of ferromagnetic thin films and nanostructures. *Science* **2014**, *345*, 1337–1340. [[CrossRef](#)] [[PubMed](#)]
8. Tauchert, S.R.; Volkov, M.; Ehberger, D.; Kazenwadel, D.; Evers, M.; Lange, H.; Donges, A.; Book, A.; Kreuzpaintner, W.; Nowak, U.; et al. Polarized phonons carry angular momentum in ultrafast demagnetization. *Nature* **2022**, *602*, 73–77. [[CrossRef](#)]
9. Philippe, S.; Quentin, R.; Sébastien, L.; Gregory, M.; Stéphane, M. Light induced ultrafast magnetization dynamics in metallic compounds. *J. Magn. Magn. Mater.* **2022**, *560*, 169596. [[CrossRef](#)]
10. Wang, S.C.; Wei, C.; Feng, Y.H.; Cao, H.K.; Li, W.Z.; Cao, Y.Y.; Guan, B.O.; Tsukamoto, A.; Kirilyuk, A.; Kimel, A.V.; et al. Dual-shot dynamics and ultimate frequency of all-optical magnetic recording on GdFeCo. *Light Sci. Appl.* **2021**, *10*, 8. [[CrossRef](#)] [[PubMed](#)]
11. Malinowski, G.; Longa, F.D.; Rietjens, J.H.H.; Paluskar, P.V.; Huijink, R.; Swagten, H.J.M.; Koopmans, B. Control of speed and efficiency of ultrafast demagnetization by direct transfer of spin angular momentum. *Nat. Phys.* **2008**, *4*, 855–858. [[CrossRef](#)]
12. Rudolf, D.; La-O-Vorakiat, C.; Battiato, M.; Adam, R.; Shaw, J.M.; Turgut, E.; Maldonado, P.; Mathias, S.; Grychtol, P.; Nembach, H.T.; et al. Ultrafast magnetization enhancement in metallic multilayers driven by superdiffusive spin current. *Nat. Commun.* **2012**, *3*, 1037. [[CrossRef](#)] [[PubMed](#)]

13. Choi, G.M.; Moon, C.H.; Min, B.C.; Lee, K.J.; Cahill, D.G. Thermal spin-transfer torque driven by the spin-dependent Seebeck effect in metallic spin-valves. *Nat. Phys.* **2015**, *11*, 576–581. [[CrossRef](#)]
14. Melnikov, A.; Razdolski, I.; Wehling, T.O.; Papaioannou, E.T.; Roddatis, V.; Fumagalli, P.; Aktsipetrov, O.; Lichtenstein, A.I.; Bovensiepen, U. Ultrafast transport of laser-excited spin-polarized carriers in Au/Fe/MgO(001). *Phys. Rev. Lett.* **2011**, *107*, 076601. [[CrossRef](#)] [[PubMed](#)]
15. Battiato, M.; Carva, K.; Oppeneer, P.M. Superdiffusive spin transport as a mechanism of ultrafast demagnetization. *Phys. Rev. Lett.* **2010**, *105*, 027203. [[CrossRef](#)]
16. Carpene, E.; Mancini, E.; Dallera, C.; Brenna, M.; Puppini, E.; De Silvestri, S. Dynamics of electron-magnon interaction and ultrafast demagnetization in thin iron films. *Phys. Rev. B* **2008**, *78*, 174422. [[CrossRef](#)]
17. Koopmans, B.; Malinowski, G.; Longa, F.D.; Steiauf, D.; Fähnle, M.; Roth, T.; Cinchetti, M.; Aeschlimann, M. Explaining the paradoxical diversity of ultrafast laser-induced demagnetization. *Nat. Mater.* **2010**, *9*, 259–265. [[CrossRef](#)]
18. Turgut, E.; Grychtol, P.; La-O-Vorakiat, C.; Adams, D.E.; Kapteyn, H.C.; Murnane, M.M.; Mathias, S.; Aeschlimann, M.; Schneider, C.M.; Shaw, J.M.; et al. Publisher's Note: Reply to "Comment on 'Ultrafast Demagnetization Measurements Using Extreme Ultraviolet Light: Comparison of Electronic and Magnetic Contributions'" [*Phys. Rev. X* **2013**, *3*, 039901. [[CrossRef](#)]
19. Peng, Y.; Shi, C.J.; Zhu, Y.M.; Gu, M.; Zhuang, S.L. Terahertz spectroscopy in biomedical field: A review on signal-to-noise ratio improvement. *Phys. Rev. Lett.* **2020**, *1*, 12. [[CrossRef](#)]
20. Peng, Y.; Huang, J.L.; Luo, J.; Yang, Z.F.; Wang, L.P.; Wu, X.; Zang, X.F.; Yu, C.; Gu, M.; Hu, Q.; et al. Three-step one-way model in terahertz biomedical detection. *Photonix* **2022**, *2*, 12. [[CrossRef](#)]
21. Kampfrath, T.; Sell, A.; Klatt, G.; Pashkin, A.; Mährlein, S.; Dekorsy, T.; Wolf, M.; Fiebig, M.; Leitenstorfer, A.; Huber, R. Coherent terahertz control of antiferromagnetic spin waves. *Nat. Photonics* **2011**, *5*, 31–34. [[CrossRef](#)]
22. Jin, Z.M.; Mics, Z.; Ma, G.H.; Cheng, Z.; Bonn, M.; Turchinovich, D. Single-pulse terahertz coherent control of spin resonance in the canted antiferromagnet YFeO₃, mediated by dielectric anisotropy. *Phys. Rev. B* **2013**, *87*, 094422. [[CrossRef](#)]
23. Nova, T.F.; Cartella, A.; Cantaluppi, A.; Forst, M.; Bossini, D.; Mikhaylovskiy, R.V.; Kimel, A.V.; Merlin, R.; Cavalleri, A. An effective magnetic field from optically driven phonons. *Nat. Phys.* **2017**, *13*, 132–136. [[CrossRef](#)]
24. Baierl, S.; Hohenleutner, M.; Kampfrath, T.; Zvezdin, A.; Kimel, A.; Huber, R.; Mikhaylovskiy, R. Nonlinear spin control by terahertz-driven anisotropy fields. *Nat. Photonics* **2016**, *10*, 715–721. [[CrossRef](#)]
25. Kampfrath, T.; Tanaka, K.; Nelson, K. Resonant and nonresonant control over matter and light by intense terahertz transients. *Nat. Photonics* **2013**, *7*, 680–690. [[CrossRef](#)]
26. Jin, Z.M.; Tkach, A.; Casper, F.; Spetter, V.; Grimm, H.; Thomas, A.; Kampfrath, T.; Bonn, M.; Kläui, M.; Turchinovich, D. Accessing the fundamentals of magnetotransport in metals with terahertz probes. *Nat. Phys.* **2015**, *11*, 761–766. [[CrossRef](#)]
27. Jin, Z.M.; Li, J.G.; Zhang, W.J.; Guo, C.Y.; Wan, C.H.; Han, X.F.; Cheng, Z.X.; Zhang, C.; Balakin, A.V.; Shkurinov, A.P.; et al. Magnetic modulation of terahertz waves via spin-polarized electron tunneling based on magnetic tunnel junctions. *Phys. Rev. Appl.* **2020**, *14*, 014032. [[CrossRef](#)]
28. Neeraj, K.; Awari, N.; Kovalev, S.; Polley, D.; Hagström, N.Z.; Arekapudi, S.S.P.K.; Semisalova, A.; Lenz, K.; Green, B.; Deinert, J.C.; et al. Inertial spin dynamics in ferromagnets. *Nat. Phys.* **2021**, *17*, 245–250. [[CrossRef](#)]
29. Vicario, C.; Ruchert, C.; Ardana-Lamas, F.; Derlet, P.M.; Tudu, B.; Luning, J.; Hauri, C.P. Off-resonant magnetization dynamics phase-locked to an intense phase-stable terahertz transient. *Nat. Photonics* **2013**, *7*, 720–723. [[CrossRef](#)]
30. Walowski, J.; Münzenberg, M. Perspective: Ultrafast magnetism and THz spintronics. *J. Appl. Phys.* **2016**, *120*, 140901. [[CrossRef](#)]
31. Beaurepaire, E.; Turner, G.M.; Harrel, S.M.; Beard, M.C.; Bigot, J.Y.; Schmuttenmaer, C.A. Coherent terahertz emission from ferromagnetic films excited by femtosecond laser pulses. *Appl. Phys. Lett.* **2004**, *84*, 3465–3467. [[CrossRef](#)]
32. Zhang, W.T.; Maldonado, P.; Jin, Z.M.; Seifert, T.S.; Arabski, J.; Schmerber, G.; Beaurepaire, E.; Bonn, M.; Kampfrath, T.; Oppeneer, P.M.; et al. Ultrafast terahertz magnetometry. *Nat. Commun.* **2020**, *11*, 4247. [[CrossRef](#)] [[PubMed](#)]
33. Kampfrath, T.; Battiato, M.; Maldonado, P.; Eilers, G.; Nötzold, J.; Mährlein, S.; Zbarsky, V.; Freimuth, F.; Mokrousov, Y.; Blügel, S.; et al. Terahertz spin current pulses controlled by magnetic heterostructures. *Nat. Nanotechnol.* **2013**, *8*, 256–260. [[CrossRef](#)]
34. Seifert, T.; Jaiswal, S.; Martens, U.; Hannegan, J.; Braun, L.; Maldonado, P.; Freimuth, F.; Kronenberg, A.; Henrizi, J.; Radu, I.; et al. Efficient metallic spintronic emitters of ultrabroadband terahertz radiation. *Nat. Photonics* **2016**, *10*, 483–488. [[CrossRef](#)]
35. Cheng, L.; Wang, X.B.; Yang, W.F.; Chai, J.W.; Yang, M.; Chen, M.J.; Wu, Y.; Chen, X.X.; Chi, D.Z.; Goh, K.E.J.; et al. Far out-of-equilibrium spin populations trigger giant spin injection into atomically thin MoS₂. *Nat. Phys.* **2019**, *15*, 347. [[CrossRef](#)]
36. Huisman, T.J.; Mikhaylovskiy, R.V.; Costa, J.D.; Freimuth, F.; Paz, E.; Ventura, J.; Freitas, P.P.; Blügel, S.; Mokrousov, Y.; Rasing, T.; et al. Femtosecond control of electric currents in metallic ferromagnetic heterostructures. *Nat. Nanotechnol.* **2016**, *11*, 455. [[CrossRef](#)]
37. Zhou, C.; Liu, Y.P.; Wang, Z.; Ma, S.J.; Jia, M.W.; Wu, R.Q.; Zhou, L.; Zhang, W.; Liu, M.K.; Wu, Y.Z.; et al. Broadband terahertz generation via the interface inverse Rashba-Edelstein effect. *Phys. Rev. Lett.* **2018**, *121*, 086801. [[CrossRef](#)]
38. Jungfleisch, M.B.; Zhang, Q.; Zhang, W.; Pearson, J.E.; Schaller, R.D.; Wen, H.D.; Hoffmann, A. Control of terahertz emission by ultrafast spin-charge current conversion at Rashba interfaces. *Phys. Rev. Lett.* **2018**, *120*, 207207. [[CrossRef](#)]
39. Shen, J.H.; Feng, Z.; Xu, P.C.; Hou, D.Z.; Gao, Y.; Jin, X.F. Spin-to-charge conversion in Ag/Bi bilayer revisited. *Phys. Rev. Lett.* **2021**, *126*, 197201. [[CrossRef](#)]

40. Zhang, Q.; Luo, Z.Y.; Li, H.; Yang, Y.M.; Zhang, X.H.; Wu, Y.H. Terahertz emission from anomalous Hall effect in a single-layer ferromagnet. *Phys. Rev. Appl.* **2019**, *12*, 054027. [[CrossRef](#)]
41. Bulgarevich, D.S.; Akamine, Y.; Talara, M.; Mag-usara, V.; Kitahara, H.; Kato, H.; Shihara, M.; Tani, M.; Watanabe, M. Terahertz magneto-optic sensor/imager. *Sci. Rep.* **2020**, *10*, 1158. [[CrossRef](#)]
42. Chen, S.C.; Feng, Z.; Li, J.; Tan, W.; Du, L.H.; Cai, J.W.; Ma, Y.C.; He, K.; Ding, H.F.; Zhai, Z.H.; et al. Ghost spintronic THz-emitter-array microscope. *Light Sci. Appl.* **2020**, *9*, 99. [[CrossRef](#)]
43. Turgut, E.; La-o-vorakiat, C.; Shaw, J.M.; Grychtol, P.; Nembach, H.T.; Rudolf, D.; Adam, R.; Aeschlimann, M.; Schneider, C.M.; Silva, T.J.; et al. Controlling the competition between optically induced ultrafast spin-flip scattering and spin transport in magnetic multilayers. *Phys. Rev. Lett.* **2013**, *110*, 197201. [[CrossRef](#)]
44. Huisman, T.J.; Mikhaylovskiy, R.V.; Tsukamoto, A.; Rasing, T.; Kimel, A.V. Simultaneous measurements of terahertz emission and magneto-optical Kerr effect for resolving ultrafast laser-induced demagnetization dynamics. *Phys. Rev. B* **2015**, *92*, 104419. [[CrossRef](#)]
45. Wu, Y.; Elyasi, M.; Qiu, X.P.; Chen, M.J.; Liu, Y.; Ke, L.; Yang, H. High-performance THz emitters based on ferromagnetic/nonmagnetic heterostructures. *Adv. Mater.* **2017**, *29*, 1603031. [[CrossRef](#)]
46. Schneider, R.; Fix, M.; Bensmann, J.; de Vasconcellos, S.M.; Albrecht, M.; Bratschitsch, R. Spintronic GdFe/Pt THz emitters. *Appl. Phys. Lett.* **2019**, *115*, 152401. [[CrossRef](#)]
47. Cramer, J.; Seifert, T.; Kronenberg, A.; Fuhrmann, F.; Jakob, G.; Jourdan, M.; Kampfrath, T.; Kläui, M. Complex terahertz and direct current inverse spin hall effect in YIG/Cu_{1-x}Ir_x bilayers across a wide concentration range. *Nano Lett.* **2018**, *18*, 1064–1069. [[CrossRef](#)]
48. Johnson, P.B.; Christy, R.W. Optical constants of transition metals: Ti, V, Cr, Mn, Fe, Co, Ni, and Pd. *Phys. Rev. B* **1974**, *9*, 5056–5070. [[CrossRef](#)]
49. Zhang, S.N.; Zhu, W.H.; Li, J.G.; Jin, Z.M.; Dai, Y.; Zhang, Z.Z.; Ma, G.H.; Yao, J.Q. Coherent terahertz radiation via ultrafast manipulation of spin currents in ferromagnetic heterostructures. *Acta Phys. Sin.* **2018**, *67*, 197202. [[CrossRef](#)]
50. Zhang, S.N.; Jin, Z.M.; Liu, X.M.; Zhao, W.Y.; Lin, X.; Jing, C.; Ma, G.H. Photoinduced terahertz radiation and negative conductivity dynamics in Heusler alloy Co₂MnSn film. *Opt. Lett.* **2017**, *42*, 3080. [[CrossRef](#)]
51. Liu, Y.S.; Cheng, H.Y.; Xu, Y.; Vallobra, P.; Eimer, S.; Zhang, X.Q.; Wu, X.J.; Nie, T.X.; Zhao, W.S. Separation of emission mechanisms in spintronic terahertz emitters. *Phys. Rev. B* **2021**, *104*, 064419. [[CrossRef](#)]
52. Mueller, B.Y.; Roth, T.; Cinchetti, M.; Aeschlimann, M.; Rethfeld, B. Driving force of ultrafast magnetization dynamics. *New J. Phys.* **2021**, *13*, 123010. [[CrossRef](#)]
53. Rouzegar, R.; Brandt, L.; Nadvornik, L.; Reiss, D.A.; Chekhov, A.L.; Gueckstock, O.; In, C.; Wolf, M.; Seifert, T.S.; Brouwer, P.W.; et al. Laser-induced terahertz spin transport in magnetic nanostructures arises from the same force as ultrafast demagnetization. *Phys. Rev. B* **2022**, *106*, 144427. [[CrossRef](#)]
54. Jiménez-Cavero, P.; Gueckstock, O.; Nádvořník, L.; Lucas, I.; Seifert, T.S.; Wolf, M.; Rouzegar, R.; Brouwer, P.W.; Becker, S.; Jakob, G.; et al. Transition of laser-induced terahertz spin currents from torque- to conduction-electron-mediated transport. *Phys. Rev. B* **2022**, *105*, 184408. [[CrossRef](#)]
55. Zhang, W.T.; Turchinovich, D. Rigorous signal reconstruction in terahertz emission spectroscopy. *Opt. Express* **2021**, *29*, 24411–24421. [[CrossRef](#)] [[PubMed](#)]
56. Faure, J.; Van Tilborg, J.; Kaïndl, R.A.; Leemans, W.P. Modelling laser-based table-top THz sources: Optical rectification, propagation and electro-optic sampling. *Opt. Quantum Electron.* **2004**, *36*, 681–697. [[CrossRef](#)]
57. Georg, S.; Bikash, D.M.; Evangelos, T.P. Charge dynamics in spintronic THz emitters. *arXiv* **2021**, arXiv:2208.07616. [[CrossRef](#)]
58. Yang, Y.S.; Dal Forno, S.; Battiato, M. Transfer-matrix description of heterostructured spintronics terahertz emitters. *Phys. Rev. B* **2022**, *104*, 155437. [[CrossRef](#)]
59. Agarwal, P.; Yang, Y.S.; Lourembam, J.; Medwal, R.; Battiato, M.; Singh, R. Terahertz spintronic magnetometer (TSM). *Appl. Phys. Lett.* **2022**, *120*, 161104. [[CrossRef](#)]
60. Jin, Z.M.; Peng, Y.; Ni, Y.Y.; Wu, G.J.; Ji, B.Y.; Wu, X.; Zhang, Z.Z.; Ma, G.H.; Zhang, C.; Chen, L.; et al. Cascaded amplification and manipulation of terahertz emission by flexible spintronic heterostructures. *Laser Photonics Rev.* **2022**, *16*, 2100688. [[CrossRef](#)]